




MOFs-derived synthesis of Ni-doped ZnO nanostructured material towards excellent *N*-butanol sensing performance and long-term stability

Shengsen Pan¹, Yun Guo^{1,*} , Gang Chen¹, Lili Sun¹, Jian Huang¹, Linjun Wang¹, Lingli Cheng², and Zheng Jiao^{2,*}

¹School of Materials Science and Engineering, Shanghai University, Shanghai 200444, China

²Key Laboratory of Organic Compound Pollution Control Engineering, Ministry of Education, Shanghai University, Shanghai 200444, China

Received: 22 October 2021

Accepted: 31 January 2022

Published online:

21 February 2022

© The Author(s), under exclusive licence to Springer Science+Business Media, LLC, part of Springer Nature 2022

ABSTRACT

The nanometallic oxides were designed as precursors and the organic substances as ligands, selecting the facile uniform co-precipitation and hydrothermal as preparing methods, the bimetallic organic framework materials (MOF:Ni-ZIF-8) were synthesized with doping different weight of Ni metal elements. The series of ZnO-MOF nanostructures (pure MOF-ZnO, 1% Ni-ZnO, 3% Ni-ZnO, 5% Ni-ZnO, 7% Ni-ZnO, 9% Ni-ZnO) have been achieved after calcination. The structural, morphological and surface electronical features were characterized by XRD, SEM, BET, UV-Vis, XPS and EIS. By using the WS-30A measurement system, the gas sensitive performances of as-prepared materials were tested and analyzed, the effect of Ni dopant was discussed. The results showed that the surface area of 5% Ni doped ZnO achieved 20.248 cm²/g with 49.27% exceeding than that of pure MOF-ZnO, and the banding width reduced by 0.041 eV with more oxygen vacancies of 3.88%. Meanwhile, the 5% Ni-ZnO device was much more sensitive to 100 ppm *N*-butanol up to 138.49, with more advantageous long-term stability and short-term response recovery. Therefore, the introduction of Ni dopant has exerted a certain impact on carrier migration rate and transport performance to produce more oxygen vacancies, which is of great significance towards the preparation of high-efficiency ZnO-based gas sensor.

Address correspondence to E-mail: guoyun@shu.edu.cn; zjiao@shu.edu.cn

1 Introduction

Nowadays, while people's living standards have improved significantly, the technological development has also brought about a series of environmental problems. The exhaust gases emitted during industrial production have released large quantities of volatile organic compounds (VOCs), such as benzene, toluene, xylene, *N*-butanol, triethylamine, acetone, formaldehyde, etc. [1, 2], incurring major components of atmospheric pollution (ozone layer depletion, acid rain, photochemical smog phenomenon, etc.). The human body accidentally inhaled high concentrations of VOCs gas in the environment can easily cause acute poisoning, the lighter ones may suffer from headache, dizziness, coughing, nausea, or vomiting, the heavier ones may arouse liver poisoning or even rapid coma, as some may induce life-threatening consequences [3, 4]. *N*-butanol, a colorless, transparent liquid with a pungent odor, is an important chemical mainly used in the preparation of surfactants, plasticizers, and some alcohols, which is also a solvent for paints and an extractant for chemical products. Only 50 ppm of *N*-butanol can make people feel drowsy and dizzy, and cause serious damage to the respiratory system [5–7]. Therefore, it is vitally important to be able to swiftly and accurately detect the presence of trace amounts of *N*-butanol in the environment. Therefore, it will make much significance to develop an inexpensive and effective gas sensor for detecting *N*-butanol.

Numerous sensors have been used for the detection of VOCs gases in the past decades, such as metal oxide semiconductor (MOS) sensors, electrochemical sensors, thermal conductivity sensors and so on. Among them thermal conductivity sensors are the common method for detecting *N*-butanol. However, the disadvantages such as high cost, long response-time, and complicated operation make them not adaptable for wide-scale use [8], while MOSs have received a lot of attention in the field of gas sensing due to their low cost, better chemical and thermal stability, excellent gas-sensing performance, and ease of fabrication [9–12]. MOS can be divided into n-type and p-type, n-type MOS mainly take electrons as carriers, such as ZnO [13], SnO₂ [14], Fe₂O [15], TiO₂ [16], etc. While most of the carriers of p-type MOS are holes, mainly including Co₃O₄ [17], NiO [18], and the others. And n-type MOS are more widely studied

and gradually applied owing to their higher sensitivity and faster response time.

ZnO is a direct broadband n-type semiconductor material, intensively studied and extensively investigated for conducting as photocatalysts, conductive and sensitive materials [19, 20], due to its relative performances, ease of fabrication, non-toxicity, low cost and good thermal and chemical stability, which is nowadays considered as the gas sensing material with most great potential for development [21, 22]. Meanwhile, metal–organic framework materials (MOFs), the relatively novel type of materials in recent years, are a class of crystalline materials consisting of metal ions and organic ligands (mostly containing carboxyl groups or nitrogen heterocycles) self-assembled by coordination to form 1D, 2D or 3D reticular skeleton with periodic cycles, which possess abundant pore structure, huge specific surface area. Since MOFs introduction, they have been mostly utilized as templates to design and synthesize unique materials, as the change of organic ligands can effectively modulate the morphology, the pore size, specific surface area and other parameters [23]. Nevertheless, most of the MOFs materials cannot be directly implemented for gas sensors at present because most of them are not conductive, but after high-temperature calcination, it is possible to obtain MOFs-derived materials (oxides of the corresponding metal ion ligands), which maintain the MOFs structural framework and allow the application in gas sensors, such processing has attracted strong interest from worldwide researchers. Nanostructured ZnO with intricate surface structures and potential advantages, such as MOF-derived hollow cages [24, 25], micro-flower [26] and nanosheets [27], have been synthesized taking use of MOFs as templates to improve the sensor properties for detecting various VOCs gases in current literatures. However, many drawbacks yet remain, such as insufficient lower detection limit and high response temperature [28]. Recently, many research results have demonstrated that doped MOS materials presenting superior sensitive properties than single-oxide semiconductor materials. Therefore, more and more efforts are requisite to be taken in the study of MOS doping for highly efficient sensor characterization [29–31].

In this work, we first prepared ZIF-8 (a species of MOF) by homogeneous co-precipitation method, then doped MOF with different amount of Ni contents by hydrothermal method, and finally obtained a

series of Ni-doped ZnO nanomaterials after calcination at 500 °C using Ni-ZIF-8 as the template. Via performance tests, it was approved that the 5% Ni-doped ZnO achieved the most optimal response to *N*-butanol and long-term stability. This can be attributed to its possession of larger specific surface area, smaller forbidden band width and more abundant oxygen vacancies. Thus, our work have provided a facile route for the realization of metal-doped MOF gas-sensitive materials with stable performance, advantageous selectivity and high responsiveness.

2 Experimental section

2.1 Materials and synthesis

All chemical reagents used in this experiment were analytical grade without further purification. All the reagents were purchased from Sinopharm Chemical Reagent Co. Ltd of China. Methanol as a solvent was used throughout the experiment.

The preparation process can be briefly described as follows: 6.25 mmol 2-methylimidazole and 1.57 mmol Zinc nitrate hexahydrate [$\text{Zn}(\text{NO}_3)_2 \cdot 6\text{H}_2\text{O}$, 99%] were dispersed into 40 mL of methanol solution, stirred for 10 min at room temperature to obtain a clarified solution, then the $\text{Zn}(\text{NO}_3)_2 \cdot 6\text{H}_2\text{O}$ solution was rapidly poured into the 2-methylimidazole and continued to stir for 5 min. The mixed solution was left to precipitate at room temperature for 24 h. The precipitated product was separated by centrifugation and washed several times with methanol solution, and then the centrifuged sample was placed in a drying oven at 70 °C overnight. After drying, solid ZIF-8 was gained and placed in a muffle furnace at the calcination temperature of 500 °C for 2 h, the required white ZnO powder was thus finally obtained.

For considered Ni-doped ZnO nanomaterials, ZIF-8 was previously synthesized by the above-mentioned homogeneous co-precipitation method. Devising certain amount of Zn^{2+} with different contents of $\text{Ni}(\text{NO}_3)_2 \cdot 6\text{H}_2\text{O}$ (1 wt%, 3 wt%, 5 wt%, 7 wt%, and 9 wt%, denoted as weight percent of Ni doped ZnO series) were added to 10 ml of methanol solution and stirred for 10 min, then the above solution was poured into the ZIF-8 solution and went on stirring for 3 min. After that, the mixed solution was transferred to a 100 ml of Teflon-lined stainless steel

autoclave and placed in an oven at a constant temperature of 120 °C for 4 h. The resulting white-green product was collected and purified by centrifugation with a few times of methanol washes, then was dried overnight in an oven at 70 °C. The next day, the prepared material was heated in a tube furnace at the heating rate of 1 °C/min and kept at 500 °C for 2 h by natural cooling. Finally, the porous structured Ni-ZnO nanoparticles were successfully materialized. The whole preparation process is depicted at length in Fig. 1.

2.2 Characterization

The phase composition and the crystalline structure of the above-prepared samples were analyzed by X-ray diffraction (XRD, D/MAX2200V PC, Cu $K\alpha_1$, $\lambda = 1.5406 \text{ \AA}$, Rigaku, Japan), with the scanning range from 10 to 90 °C. Both morphology and microstructure were investigated by an environmental scanning electron microscope (SEM, Philips XL-30, Netherlands). The adsorption-desorption isotherms of nitrogen measurement were acted on an automated surface analyzer (Quantachrome, Quadrasord SI, USA). Moreover, surface area and pore size distribution were estimated by Brunauer-Emmett-Teller (BET) and Barrett-Joyner-Halenda (BJH) methods, respectively. The chemical composition evaluation was implemented by X-ray photoelectron spectroscopy (XPS, Thermo, ESCALAB 250XI, USA). The optical properties were surveyed by UV-Vis spectrometer (UV, UV-3600, Japan) from 200 to 800 nm, with the band gap widths deduced by the Kubelka-Munk equation. The Chenhua CHI 660E electrochemical analyzer were utilized for the electrochemical impedance spectroscopy (EIS) testaments.

2.3 Fabrication and performance testing of gas sensors

The fabrication steps of this sensor were similar to previous reports [32, 33]. The samples of pure MOF-ZnO and Ni-ZnO doped with different contents were all mixed with appropriate amount of ethanol and ground into a homogeneous paste respectively, then uniformly coated on the surface of the hollow ceramic tube (0.8 mm inner diameter, 1.2 mm outer diameter, 4 mm length, with a pair of Au electrodes and 4 Pt wires printed on both ends of the tube for soldering to the pedestal of the gas-sensitive

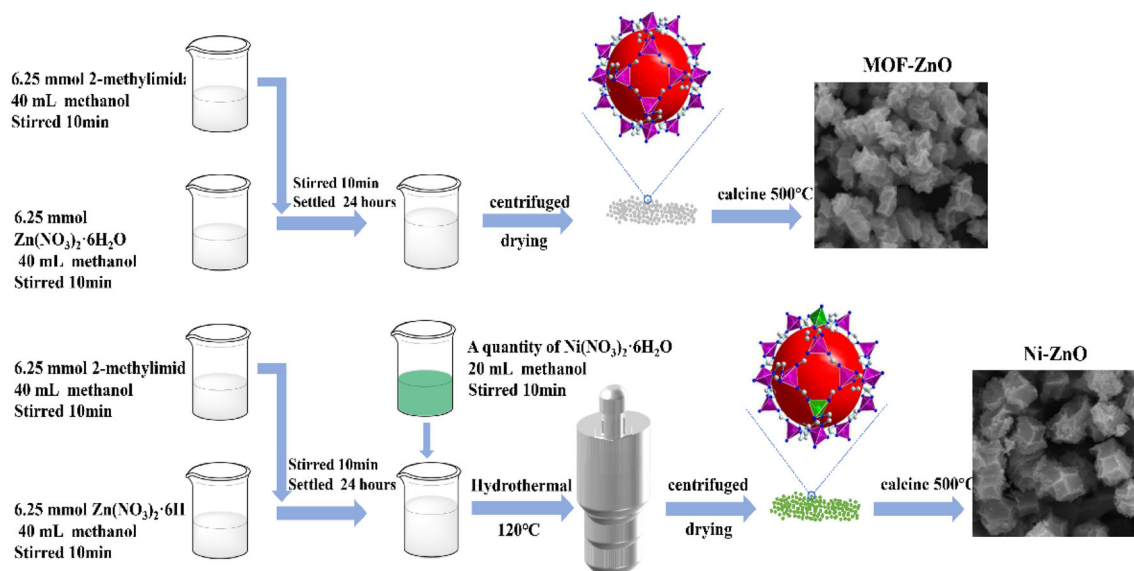
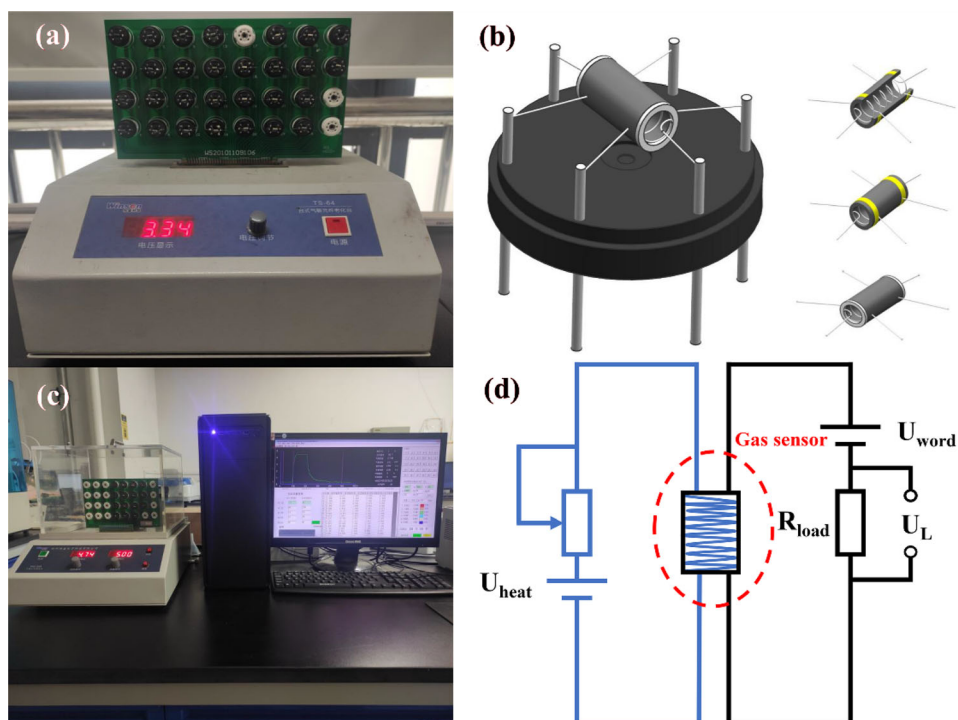


Fig. 1 Schematic diagram of synthetic process

assembly). The above-prepared samples were completely covered two Au electrodes on the surface of Al_2O_3 ceramic tube. Subsequently, the as-coated Al_2O_3 ceramic tubes were placed in an oven and dried at 80°C for 2 h, with the aim of removing the ethanol effect on the sensors. Finally, the Ni–Cr heating wire was passed through the center of the Al_2O_3 ceramic tube and soldered to the sensor base to

form a complete gas-sensitive sensor device. The soldered gas sensors were inserted into the circuit board and the Pt wire was heated, and the sensor was allowed to place on the aging equipment (TS64, Zhengzhou Winsen Electronic Technology Co., Ltd) for 3 days at the temperature of 300°C . The aging process was done to improve the stability of the sensing performance. The aging equipment is

Fig. 2 **a** Digital photograph of gas sensor aging equipment, **b** Structure diagram of gas sensor, **c** Digital photograph of the gas sensor test system and **d** the circuit diagram of gas sensing test



photographed in Fig. 2a and the structure of the conductive gas sensor is sketched in Fig. 2b. The sensing performance was measured with WS-30A gas sensor measurement system (Zhengzhou Winsen Electronics Technology Co., Ltd), as shown in Fig. 2c. The data was collected and analyzed through an application computer software. The operating voltage of the test system was 5.0 V which was controlled by using a load resistor card to divide the voltage on the gas sensor and by adjusting the voltage of the heating wire, as the heating voltage was devised to range from 3.54 to 5.29 V, Fig. 2d depicts the circuit diagram of the gas test system. Throughout the test, the air humidity was controlled at 40% as the ambient temperature was 25 °C. In this work, the gas sensor response is defined as $S = R_a/R_g$, where R_a represents the resistance of the sensor in a steady state in air and R_g represents the resistance of the sensor in a steady state in the test gas. For n-type semiconductors, the response value refers to the ratio of the resistance of the material in air to the resistance of the material in the target gas [34]. In addition, the response time (τ_{resp}) and recovery time (τ_{rec}) are the time required for the sensor to reach 90% of the total resistance change at equilibrium during adsorption and desorption of the target gas, respectively [35].

3 Results and discussion

3.1 Structure and micromorphology analysis

Fig. S1 is the tested XRD pattern of ZIF-8 compared with the simulated ZIF-8 pattern. The comparative analysis of the diffraction data was based on the JADE software. The results show that the peak positions of the obtained ZIF-8 well correspond to the that of ZIF-8 reported in the literatures, and no impurity peaks appear, indicating the required MOF materials with preferable crystallinity have been successfully prepared [36]. Figure 3a depicts the compared XRD patterns of pure MOF-ZnO, 1% Ni-ZnO, 3% Ni-ZnO, 5% Ni-ZnO, 7% Ni-ZnO, 9% Ni-ZnO and the referential standard ZnO PDF card, all the main peaks of pure MOF-ZnO to 9% Ni-ZnO are well corresponding to that of hexagonal crystalline Wurtzite structure and no excess peaks appear suggesting the high purity and maybe the tiny amount of Ni dopant not enough to significantly modify the

crystal structure, at the same time, the sharp diffraction peaks suggesting the high crystallinity of the prepared samples. The main diffraction peaks and crystal planes of pure MOF-ZnO position at 32.05°(100), 34.66°(200), 36.50°(101), 47.86°(102), 56.85°(110), 63.10°(103) and 69.35°(112), which are consistent with the international standard card (JCPDS:70-2551). The partial enlarged views of pure MOF-ZnO and 5% Ni-ZnO from 30° to 38° are comparatively presented in Fig. 3b, it can be seen that the diffraction peaks of 5% Ni-ZnO shift to the large angle direction as a whole with respect to pure MOF-ZnO, while the diffraction peak of (101) crystal plane shifting by about 0.047°, which may attribute to partial substitution of Zn^{2+} (0.74 Å) by Ni^{2+} (0.69 Å) with smaller ionic radius [37], and concurrently confirm that Ni content has been successfully doped into ZnO lattice.

Moreover, the average crystallite sizes of pure MOF-ZnO and Ni-doped ZnO were estimated according to Scherer's formula [38] and listed in Table 1 (based on the most intensive (101) surface). It is easy to see the effect on crystal growth of Ni^{2+} doping. In general, the Ni^{2+} dopant leads to a decrease in the crystal size due to the substitution of Zn^{2+} by the smaller ionic radius Ni^{2+} , which is also identical with what was stated above. Notably the abnormal value of 9% Ni-ZnO may be caused by the excessive amount of doped Ni^{2+} , which makes it to be merely adsorbed on the surface of ZIF-8 and affects its doping into the crystal lattice.

In Fig. 4a and b, microscopic images of ZIF-8 and 5% Ni-ZIF-8 are particularly observed. It can be seen that the Ni-doped product still keeps the typical and well-defined rhombic dodecahedral structure of ZIF-8 with good dispersion, but appearing a reduction in the size of the MOF crystal. The inset of Fig. 4a yields a size of 670 nm for ZIF-8, as the size of 600 nm for 5% Ni-ZIF-8 in inset of Fig. 5b, which stays the same with the XRD analysis in virtue of the size reduction caused by the partial substitution of Zn^{2+} by smaller-sized Ni^{2+} in the ZnO lattice. And the EDS elemental surface scan of the area framed by the dashed line in Fig. 4b reveals that the presence of Zn and Ni elements (Fig. 4e and f). In Fig. 4c, the 5% Ni-ZIF-8 transformed to 5% Ni-ZnO after calcination results in a collapsed and reduced structure because the organic components of the precursor were burned off. Figure 4d presents that the size of calcinated 5% Ni-ZnO approaches about 220 nm, which is reduced

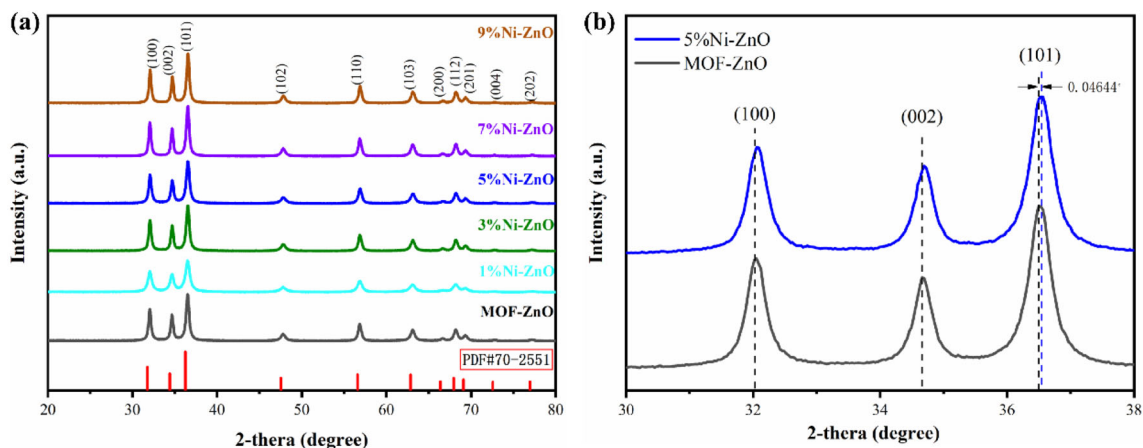


Fig. 3 a XRD patterns of pure MOF-ZnO, 1% Ni-ZnO, 3% Ni-ZnO, 5% Ni-ZnO, 7% Ni-ZnO, 9% Ni-ZnO and referential ZnO, b XRD migration comparison of MOF-ZnO and 5% Ni-ZnO.

Table 1 The average crystallite sizes of the prepared samples with different Ni contents

Sample	Crystallite size (nm)	Sample	Crystallite size (nm)
Pure MOF-ZnO	22	5% Ni-ZnO	20
1% Ni-ZnO	21	7% Ni-ZnO	20
3% Ni-ZnO	21	9% Ni-ZnO	21

Based on (101) surface

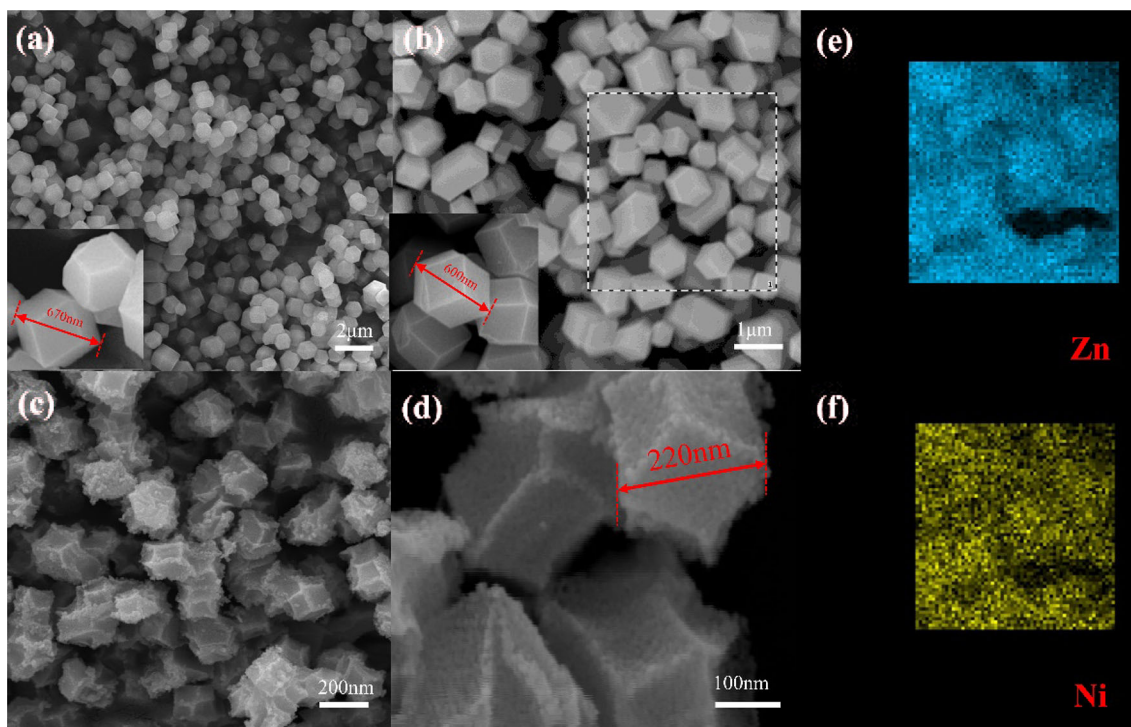


Fig. 4 SEM images of a ZIF-8 and b 5% Ni-ZIF-8, c, d 5% Ni-ZnO, and e, f EDX images of 5% Ni-ZnO.

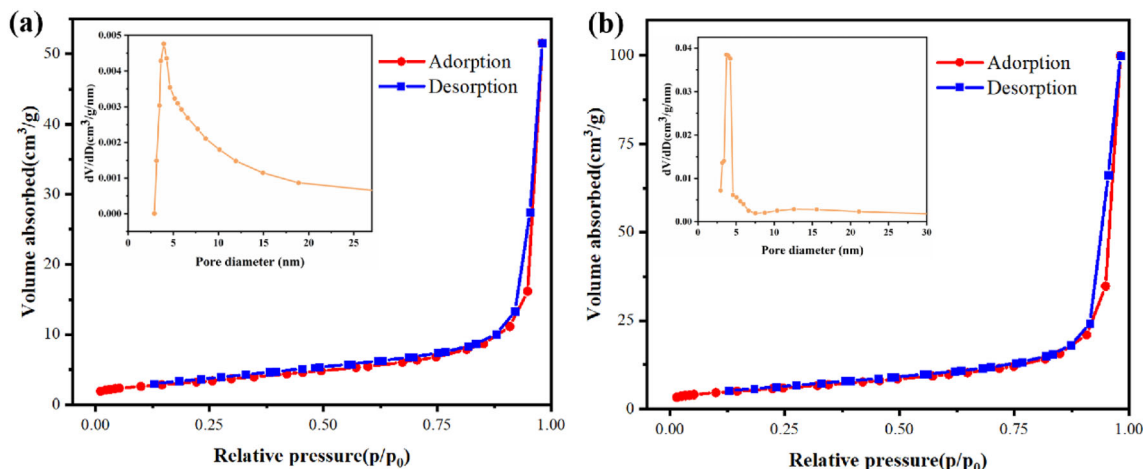


Fig. 5 Nitrogen adsorption–desorption isotherms and pore size distribution (inset): **a** MOF–ZnO and **b** 5% Ni–ZnO.

by 280 nm compared with that before calcination, and appears in mesoporous micro-cage structure composed of nanoparticles.

3.2 Surface, bandwidth and electrochemical analysis

In order to further explore the structural properties of the prepared pure MOF–ZnO and 5% Ni–ZnO materials, nitrogen adsorption–desorption isotherm measurements were performed to characterize their surface area and average pore size. The results are shown in Fig. 5 (inset for pore size distribution) and are well in accord with the typical “Type IV” isotherms with H3 hysteresis loops defined in Brunauer’s classification [39], which indicates that the prepared materials are mesoporous in structure and match the SEM observations. In addition, the specific surface area and average pore size distribution were calculated as 10.271 m²/g and 3.951 nm (Fig. 5a), while 5% Ni–ZnO reaching 20.248 m²/g and 3.734 nm (Fig. 5b), may provide a more spacious interface for superior gas-sensitive performance. Moreover, the smaller pore size of 5% Ni–ZnO than that of pure MOF–ZnO may be correlated to the reducing crystal structure size after doping, which brings into correspondence with the analytical results of XRD and SEM.

The UV–Vis absorption spectra are shown in Fig. 6 to calculate the energy band variations. In Fig. 6a, a clear absorption band can be observed near 395 nm with a slight red shift of the Ni-doped ZnO compared to the pure MOF–ZnO. The band gaps (E_g) between conduction band and valence band were calculated

by the wavelength value corresponding to intersection point using Eq. (1):

$$\alpha hv = A(hv - E_g)^{\frac{1}{2}} \quad (1)$$

The band gap energy were estimated from the above relation, where E_g corresponds to band gap energy (eV), α is the absorption coefficient, A is a constant, h is the Planck’s constant (6.626×10^{-34} J s), ν is the incident photon frequency, and the band gap for various samples are converted in Fig. 6b and listed Table 2. The E_g values diminish continuously with the increment of doped Ni content, which indicates that doping Ni can reduce the band gap of ZnO and make it easier for the electrons in the valence band jumping to the conduction band to generate more free electrons, thus can accelerate the reaction for the matrix material with the target gas for sensitivity application [40].

Pure MOF–ZnO and 5% Ni–ZnO were also subjected to XPS analysis to further investigate the electronic states of the surface elements. The panoramic spectra exhibit the existence of Zn, O and C elements in the pure MOF–ZnO sample, while Zn, Ni, O and C elements present in the 5% Ni–ZnO sample (Fig. 7a), further affirming the perfect doping of Ni into ZnO. The C element can be interpreted as the carbon-based contaminants when exposed during the testing, and the binding of the C 1s peak at 284.88 eV (Fig. S2) can be assigned as a reference for calibration [41]. Figure 7b records the high-resolution spectrum of Ni 2p with the fitting peak at 853.3 eV attributed to Ni 2p_{3/2}, and the peak fitted at 871.9 eV corresponds to Ni 2p_{1/2} [42], directing the existence of Ni²⁺. Figure 7c

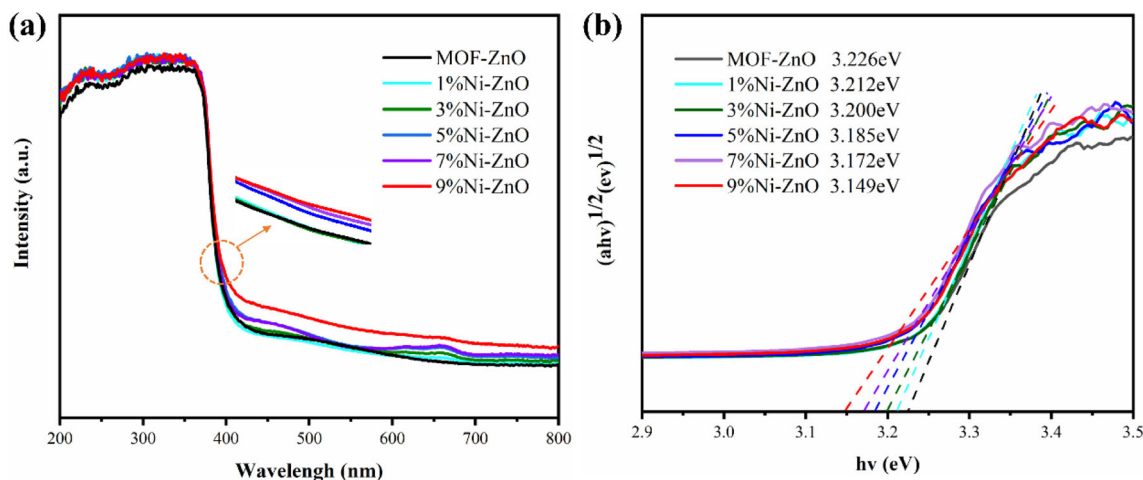


Fig. 6 **a** UV-Vis spectrums and **b** forbidden band width of pure MOF-ZnO, 1% Ni-ZnO, 3% Ni-ZnO, 5% Ni-ZnO, 7% Ni-ZnO, 9% Ni-ZnO.

Table 2 Band gap of the prepared samples with different Ni contents

Sample	Band gap (eV)	Sample	Band gap (eV)
Pure MOF-ZnO	3.226	5% Ni-ZnO	3.185
1% Ni-ZnO	3.212	7% Ni-ZnO	3.172
3% Ni-ZnO	3.200	9% Ni-ZnO	3.149

and d show the profiles of pure MOF-ZnO and 5% Ni-ZnO O 1s, with the high intensity peaks at 529.68 eV and 529.88 eV corresponding to the lattice oxygen (O_L) respectively, which can be understood in views of the different chemical environment of the O element in 5% Ni-ZnO compared to that of pure MOF-ZnO, as both featured peaks existed some minor deviations [43]. The O 1s peak at 530.9 eV and the broad peak at 532.0 eV are separately associated with the oxygen vacancy (O_V) and chemisorbed oxygen (O_C) [44]. In addition, the calculated proportions of O_V and O_C in the ZnO samples are 17.69 and 13.07%, respectively, as for 5% Ni-ZnO, they are 21.57% and 14.28%, which will provide more active sites for the target gas largely able to improve the sensing performance [45]. Two strong peaks around 1020.6 eV and 1043.7 eV in the Zn 2p spectrum (Fig. 7e, f) can be assigned to Zn 2p_{3/2} and Zn 2p_{1/2} [46].

To further investigate the electrochemical properties of the series of samples, electrochemical impedance test analysis was performed and the resulted were shown as in Fig. 8. The inset of Fig. 8 depicts

the equivalent circuit of the EIS, where R_s , R_{ct} and CPE represent the solution resistor, the charge transfer resistor and the constant phase element respectively. It can be seen that, the electrochemical impedances of all Ni-ZnO series are smaller than those of pure MOF-ZnO, which indicated that the Ni-doped ZnO presenting better conductivity and faster resistance change rate. The higher conductivity of 7% Ni-ZnO and 9% Ni-ZnO than that of 5% Ni-ZnO may be attributed to the higher doping amount. And the lower the conductivity, the lower the electron-hole complexation rate, suggesting that the 5% Ni-ZnO can capture more oxygen ions to facilitate the gas-sensitive reaction [47].

3.3 Gas-sensing properties evaluation

The operating temperature plays an important role in the gas sensor performances. In order to probe into the optimal temperature conditions, gas sensing tests at different temperatures were performed based on pure MOF-ZnO and Ni-ZnO series materials. In consideration of previous studies [48], the testing gas in this case was selected to be *N*-butanol at a concentration of 100 ppm, the response results correlated with operating temperature are shown in Fig. 9a. Initially, all the response values increase as the temperature increasement, while the maximum peak occurs at 300 °C, when continuing to raise the temperature, the response values gradually decrease. All response curves maintain the same trend and exhibit an optimum temperature of 300 °C. This can be attributed to: When the operating temperature is

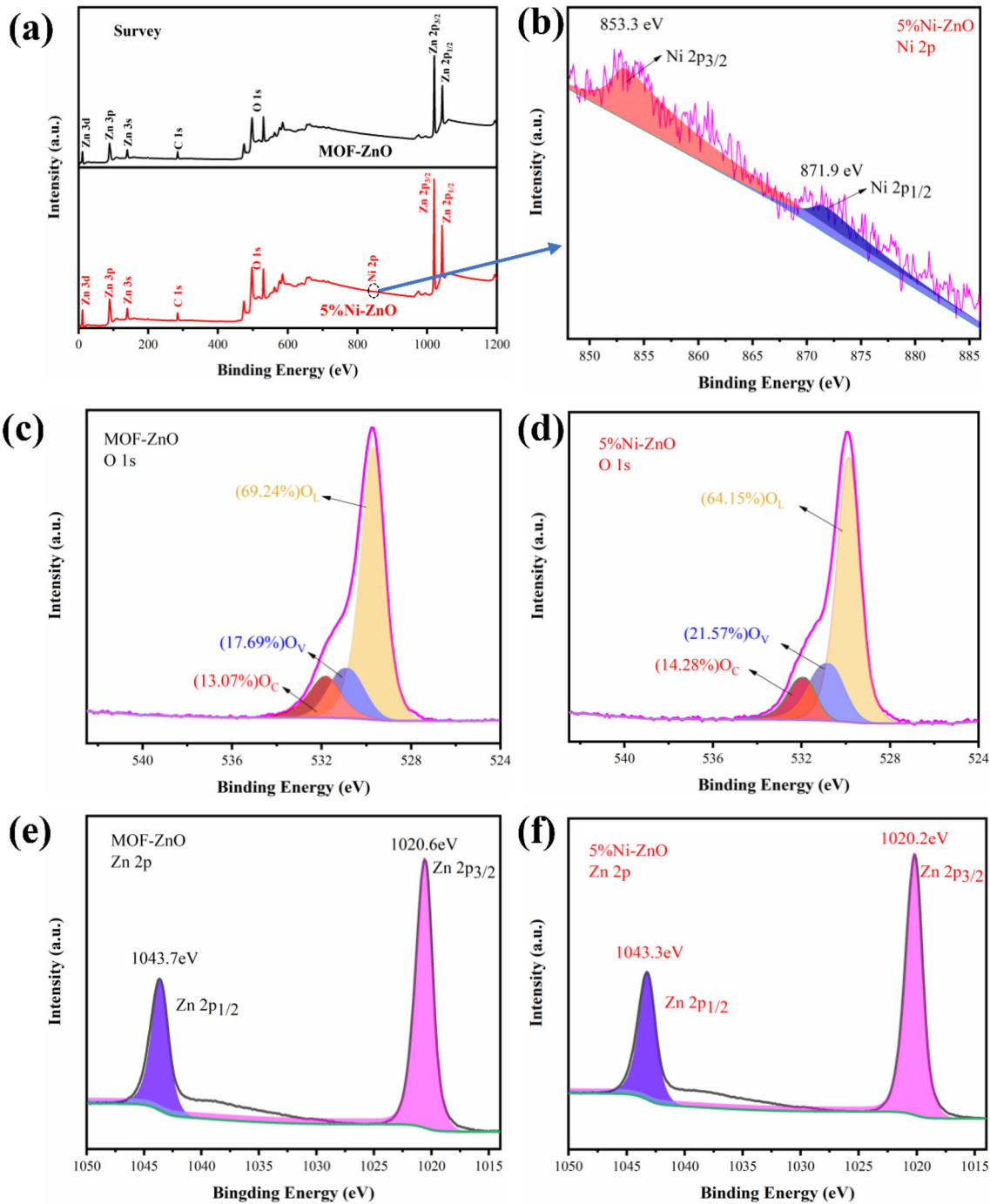


Fig. 7 XPS spectra of **a** full survey scan of MOF–ZnO, 5% Ni–ZnO, **b** Ni 2p of 5% Ni–ZnO, **c** O 1s of MOF–ZnO, **d** O 1s of 5% Ni–ZnO, **e** Zn 2p of MOF–ZnO, and **f** Zn 2p of 5% Ni–ZnO

relatively low, most *N*-butanol gases are inactive and do not possess enough activation energy to react with the oxygen adsorbed on the surface resulting in the lower responses. As the temperature elevates, the gas molecules gain more energy to overcome the activation energy barrier to improve the responses.

However, excessively high temperature will attenuate the dynamic adsorption of the target gas on the surface of the sensitive material, so it can be understood as the desorption rate of the gas molecules turns out to be greater than the corresponding adsorption rate in the cases of higher temperature,

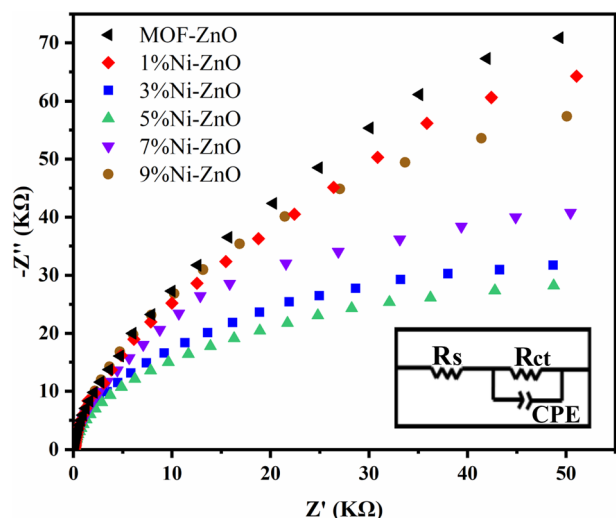


Fig. 8 The EIS Nyquist plots of pure MOF-ZnO and Ni-ZnO series

which leads to a substantial decrease in the response [4, 48]. Figure 9b shows the transient sensing curves of the six sensors for 100 ppm *N*-butanol at the optimum operating temperature of 300 °C. The 5% Ni-ZnO sample exhibits the highest response of 138.49, comparing with only 31.41 for pure MOF-ZnO. This is due to the fact that 5% Ni-ZnO possess more oxygen vacancies, a larger specific surface area and lower impedance than other samples. Compared with the remaining samples, the electrochemical impedance of 5% Ni-ZnO presents the smallest value by EIS analysis, which also indirectly confirms that 5% Ni performs the best doping content. All sensors

reflect fast response and recovery process which are essential for the practical applications.

Therefore, the 5% Ni-ZnO gas sensor with the most excellent response, attributed to the more oxygen vacancies and the larger specific surface area, was selected to be as the focus research target for the more profound investigations. The response–recovery curves for different concentrations tested at the optimum operating temperature are shown in Fig. 10a. It is obvious that larger response values are acquired under higher gas concentration conditions. The fitting curves for the response values corresponding to their different concentrations are depicted in Fig. 10b (and the inset is unfitted), the equation between them is well fitted as:

$$y = a + bx \quad (2)$$

And the correlation between the data and the fitted curve reaches 0.9986, suggesting the linear correlation with a well positive proportional relationship [4, 48]. Even as gas concentration of 1 ppm, the sensor still emerges as a good response, indicating that it is beneficial for low concentration gas detection.

In practical sensor applications, reproducibility also acts as the key indicator to assess the device performances. Therefore, the testing 5% Ni-ZnO sensor was exposed to 100 ppm of *N*-butanol at 300 °C for 6 response–recovery cycles, and the curve did not change significantly, as shown in Fig. 11a, giving the exceptional reproducibility with the response time of 32 s and the recovery time of 53 s. The desorption process appears slightly slow may due to the too high concentration of the adsorbed *N*-

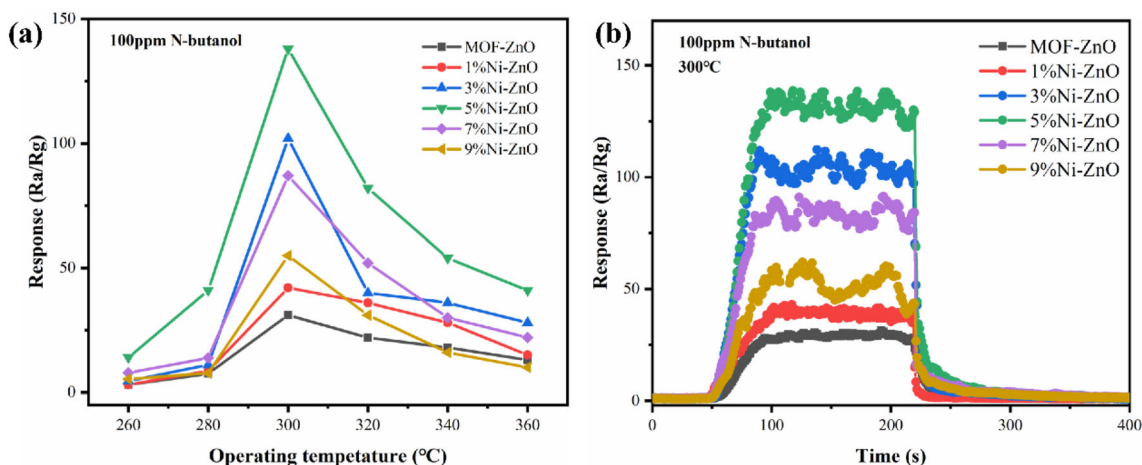


Fig. 9 **a** Responses to 100 ppm *N*-butanol of the fabricated sensors at different operating temperatures; **b** The response–recovery curves of pure MOF-ZnO and Ni-ZnO series (with different reaction times) sensors toward 100 ppm of *N*-butanol at 300 °C.

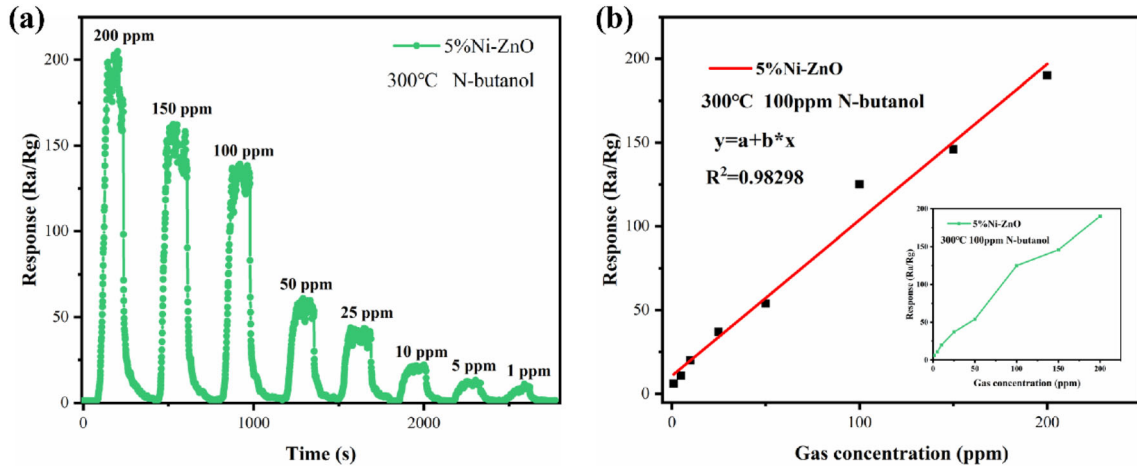


Fig. 10 a Dynamic response curves of 5% Ni–ZnO at 300 °C to different concentrations of *N*-butanol; b Fitted curves of the response of 5% Ni–ZnO to different concentrations of *N*-butanol, inset is the response to different concentrations of *N*-butanol

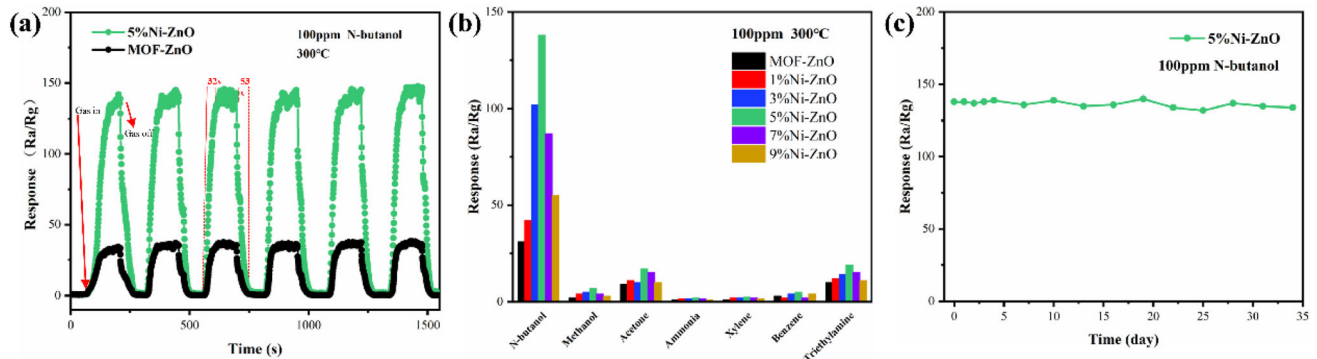


Fig. 11 a Six-cycle response–recovery curves of MOF–ZnO and 5% Ni–ZnO for 100 ppm *N*-butanol at 300 °C; b Response values of six sensors for seven different gases; c Long-term stability of 5% Ni–ZnO gas sensor for *N*-butanol at 300 °C

butanol gas. In Fig. 11b, the response values were optionally measured for 100 ppm of *N*-butanol, methanol, acetone, ammonia, xylene, benzene, and triethylamine at 300 °C. It is evident that the six gas sensors demonstrate equally prominent response to *N*-butanol, while poor sensitivity observed for the other gases, which approves that the samples take on an excellent selectivity and can make an effectively identification for *N*-butanol. This can be interpreted that *N*-butanol contains hydroxyl substances more polar than ammonia, acetone, xylene, and benzene, which able to provide more electrons. In addition, the presence of large intrinsic crystal defects and abundant oxygen vacancies in *N*-butanol facilitate more additional electrons binding as free carriers [4, 48].

Long-term stability also works as important for the enduring utility of the sensor. To evaluate the effect of daily environment on the gas sensor stability, the

5% Ni–ZnO sensor was placed in a dry room and tested continuously for 35 days (Fig. 11c). The responses fluctuated slightly throughout the test, as the value of 5% Ni–ZnO to *N*-butanol could still be maintained above 130 without any significant decrease, further indicating the good long-term stability and the good response–recovery performance. In addition, the performances of 5% Ni–ZnO sensor and other reported ZnO sensors are compared and listed in Table 3, from which the gas sensor prepared in this work achieved more distinguished response for *N*-butanol and a lower operating temperature, confirming the superior gas sensing performance with great potential for practical applications.

3.4 Gas sensing mechanism

The gas-sensing performance of metal oxides is usually subject to various influence factors such as

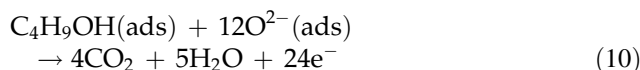
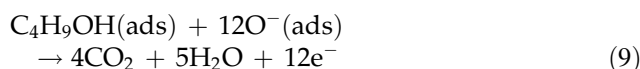
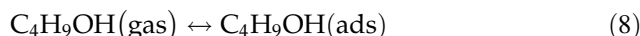
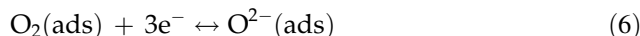
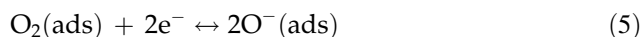
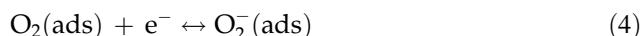
Table 3 Comparison of varied ZnO-based sensors in VOCs sensing performances

Materials	Gas	Concentration (ppm)	Working temperature (°C)	Response (R_a/R_g)	References
Core-shell ZnO@TiO ₂	<i>N</i> -butanol	100	200	7	[6]
ZnO microflowers	<i>N</i> -butanol	100	320	21.7	[7]
Hollow ZnO/Co ₃ O ₄	acetone	100	300	30.1	[9]
ZnO hollow spheres	<i>N</i> -butanol	100	382	57.6	[11]
In ₂ O ₃ /ZnO nanorods	<i>N</i> -butanol	100	370	104.3	[19]
SnO ₂ -ZnO nanowires	ethanol	100	400	14.05	[22]
Tourmaline@ZnO nanostructures	<i>N</i> -butanol	100	320	120.8	[48]
5% Ni-ZnO nanostructures	<i>N</i>-butanol	100	300	138.49	This work

The result obtain from this work is highlighted in bold

heating temperature, additional catalyst, specific surface area, and material morphology. The manner the target gas acting on the material surface plays an important role in the sensing process. The gas sensing mechanism regarding n-type metal oxides has been mainly manifested in the gas adsorption–desorption process and the alteration of the electron depletion layer induced by charge transfer. Specifically, the sensitive performances of oxide sensors are chiefly determined by the conversion in resistance created by chemisorption and desorption phenomena of oxygen in ambient air. In this study, the transition metal Ni was doped into the n-type ZnO-based sensor, which produces more oxygen vacancies and larger specific surface area than that of pure MOF–ZnO. Moreover, the unique catalytic property of Ni ion makes it well activate the oxygen molecules in air (O_{gas}), so as to enhance the activity of adsorbed oxygen (O_{ads}) and catalyze the redox reaction between adsorbed oxygen and *N*-butanol gas molecules, thus improves the response. According to the adsorption oxygen mechanism, the resistance of Ni–ZnO material is exponentially decreasing with the increase of heating temperature in air ambience, then oxygen will be attached onto the Ni–ZnO surface to form adsorbed oxygen (O_2^- , O^- , O^{2-}) and be excited by heat from the valence band to the conduction band to generate free electrons. It has been reported that while in 300 °C, the oxygen negative ions are dominated by O^- and O^{2-} [48–50], which can trap free electrons in the air causing a decrease in carrier concentration and an increase in resistance, with the reaction as in Eq. (3–6). In gas ambience at 300 °C, when coming into contact with the reducing gas *N*-butanol and reacting with the adsorbed oxygen (O^- , O^{2-}), Ni–ZnO can re-release the electrons into the conduction

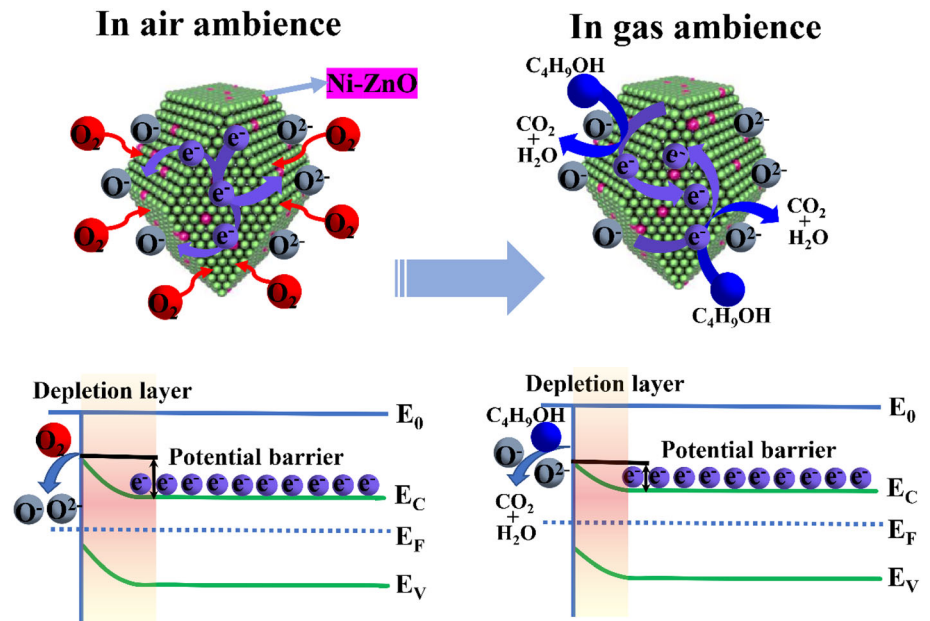
band and enhanced electrons in the conduction band, reduce the potential barriers to form a narrow depletion layer, thus make the resistance reduced as shown in the Eqs. (7–10), and the reaction mechanism has been depicted in Fig. 12.



4 Conclusions

The series of Ni–ZnO nanomaterials were prepared by homogeneous co-precipitation and hydrothermal methods taking MOF as the sacrificial template, and characterized by XRD, SEM, XPS, BET, EIS and UV–vis. The testing results showed that the Ni–ZnO micro-nano structures were more sensitive to *N*-butanol gas detection. The most responsive value of 5% Ni–ZnO sample for 100 ppm *N*-butanol at 300 °C approaches to 138.49, which is more than 4 times that of pure MOF–ZnO. The faster response–recovery time and finer long-term stability have also been realized. The exceptional gas sensing performance may be attributed to the higher adsorbed oxygen

Fig. 12 Schematic diagram of gas sensing mechanism of Ni–ZnO micro-nano sensor



concentration, larger specific surface area and richer oxygen vacancy defects in the 5% Ni–ZnO sample, which may originate from the lattice distortion initiated by the transition metal Ni doping. Thus, Ni-doped ZnO micro-nano structures have been proven to be potentially promising for the *N*-butanol sensitivity and be going to play an important role in the field of environmental detection.

Author contributions

SP for material preparation, data collection and writing original draft; YG for investigation and methodology; GC, LS for formal analysis, and writing-review & editing; JH, QZ, LC, ZJ for supervision, validation and resources.

Funding

This work is supported by the National Natural Science Foundation of China (Grant No. 21671130) and Key Laboratory of Organic Compound Pollution Control Engineering, Ministry of Education (Shanghai University, 200444, China). We are also grateful to the Instrumental analysis and Research Center (Shanghai University, Shanghai, People's Republic of China).

Data availability

The data that support the findings of this study are available within the article (and its supplementary information files).

Declarations

Conflict of interest There are no conflict to declare.

Ethical approval For this type of study, the ethical approval was not.

Supplementary Information: The online version contains supplementary material available at <http://doi.org/10.1007/s10854-022-07888-5>.

References

1. M. Wang, Z. Shen, X. Zhao, F. Duanmu, Yu. Huijun, H. Ji, J. Hazard. Mater. **371**, 352 (2019)
2. D. An, Q. Wang, X. Tong, X. Lian, Y. Zou, Y. Li, Ceram. Int. **45**, 6869 (2019)
3. J. Wang, Z. Zheng, D. An, X. Tong, Q. Zhou, Mater. Sci. Semicond. Process. **83**, 139 (2018)
4. L. Cheng, Y. He, M. Gong, X. He, Z. Ning, H. Yuc, Z. Jiao, J. Alloys Compd. **857**, 158205 (2021)
5. G. Zhang, X. Qin, Mater. Res. Bull. **48**, 3743 (2013)
6. Y. Xu, L. Zheng, C. Yang, W. Zheng, X. Liu, J. Zhang, Sens. Actuators B **310**, 127846 (2020)

7. J. Huang, Y. Wu, C. Gu, M. Zhai, K. Yu, M. Yang, J. Liu, *Sens. Actuators B* **146**, 206 (2010)
8. C.-L. Cheng, P.-Y. Che, B.-Y. Chen, W.-J. Lee, L.-J. Chien, J.-S. Chang, *Bioresour. Technol.* **113**, 58 (2012)
9. D. Zhang, Z. Yang, Z. Wu, G. Dong, *Sens. Actuators B* **283**, 42 (2019)
10. A. Jagan Mohan Reddy, N.K. Katari, P. Nagaraju, K. Hussain Reddy, M.S. Surendra Babu, *J. Mater. Sci. Mater. Electron.* **32**, 7827 (2021)
11. B. Han, X. Liu, X. Xing, N. Chen, X. Xiao, S. Liu, Y. Wang, *Sens. Actuators B* **237**, 423 (2016)
12. S. Feng, X. Jia, J. Yang, Y. Li, S. Wang, H. Song, *J. Mater. Sci. Mater. Electron.* **31**, 22534 (2020)
13. J. Buasakun, P. Srilaong, G. Chaloeipote, R. Rattanakram, C. Wongchoosuk, T. Duangthongyou, *J. Solid State Chem.* **289**, 121494 (2020)
14. K.-R. Parka, H.-B. Choa, J. Lee, Y. Song, W.-B. Kim, Y.-H. Choa, *Sens. Actuators B* **302**, 127179 (2020)
15. Q. Wei, J. Sun, P. Song, J. Li, Z. Yang, Q. Wang, *Sens. Actuators B* **317**, 128205 (2020)
16. R. Malik, V.K. Tomer, V. Chaudhary, M.S. Dahiya, S.P. Nehra, P.S. Rana, S. Duhan, *Sens. Actuators B* **239**, 364 (2017)
17. L. Liu, M. Yang, H. Zhao, Xu. Yingming, X. Cheng, X. Zhang, S. Gao, H. Song, L. Huo, *Microchim. Acta.* **186**, 184 (2019)
18. L.L. Son, N.D. Cuong, T.T. Van Thi, L.T. Hieu, D.D. Trung, N. Van Hieu, *RSC Adv.* **9**, 9584 (2019)
19. C. Gu, L. Shanshan, J. Huang, C. Shi, J. Liu, *Sens. Actuators B* **177**, 453 (2013)
20. H. Wang, Q. Li, X. Zheng, C. Wang, J. Ma, B. Yan, Z. Du, M. Li, W. Wang, H. Fa, *J. Alloys Compd.* **829**, 154453 (2020)
21. X. Gao, T. Zhang, *Sens. Actuators B* **277**, 604 (2018)
22. L. Ma, S.Y. Ma, H. Kang, X.F. Shen, T.T. Wang, X.H. Jiang, Q. Chen, *Mater. Lett.* **209**, 188 (2017)
23. Wu. Ming-Xue, Y. Wang, G. Zhou, X. Liu, *ACS Appl. Mater. Interfaces* **12**, 54285 (2020)
24. Z. Li, Y. Zhang, H. Zhang, Y. Jiang, J. Yi, *ACS Appl. Mater. Interfaces* **12**, 37489 (2020)
25. N. Zhang, L. Yan, Lu. Yang, Y. Fan, S. Guo, S. Adimi, D. Liu, S. Ruan, *Chin. Chem. Lett.* **31**, 2071 (2020)
26. W. Yang, X. Xiao, B. Fang, H. Deng, *J. Alloys Compd.* **860**, 158410 (2021)
27. J. Gao, H. Meng, Q. Hu, J. Chang, L. Feng, *Sens. Actuators B* **307**, 127580 (2020)
28. Y. Kang, F. Yu, L. Zhang, W. Wang, L. Chen, Y. Li, *Solid State Ionics.* **360**, 115544 (2021)
29. R. Mo, D. Han, C. Yang, J. Tang, F. Wang, C. Li, *Sens. Actuators B* **330**, 129326 (2021)
30. A. Katoch, R. Bhardwaj, N. Goyal, S. Gautam, *Vacuum* **158**, 249 (2018)
31. Z. Chen, Z. Lin, Y. Hong, Na. Li, Xu. Mengying, *J. Mater. Sci. Mater. Electron.* **27**, 2633 (2016)
32. Z. Jiao, D. Gao, Y. Wang, H. Zhang, *Mater. Res. Bull.* **103**, 319 (2018)
33. Z. Jiao, Y. Wang, M. Ying, Xu. Jiaqiang, Xu. Laiqiang, H. Zhang, *Mater. Chem. Phys.* **172**, 113 (2016)
34. S. Shi, F. Zhang, H. Lin, Q. Wang, E. Shi, F. Qu, *Sens. Actuators B* **262**, 739 (2018)
35. K. Zhang, Z. Lin, *J. Mater. Sci. Mater. Electron.* **32**, 17395 (2021)
36. K.S. Park, Z. Ni, A.P. Cote, J.Y. Choi, R. Huang, F.J. Uribe-Romo, H.K. Chae, M. O’Keeffe, O.M. Yaghi, *PNAS* **103**, 10186 (2006)
37. V.S. Kamble, Y.H. Navale, V.B. Patil, N.K. Desai, S.T. Salunkhe, *J. Mater. Sci. Mater. Electron.* **32**, 2219 (2021)
38. H. Benelmadjat, N. Touka, B. Harieche, B. Boudine, O. Halimi, M. Sebais, *Opt. Mater. X.* **32**, 764 (2010)
39. Q. Dong, H. Su, J. Xu, D. Zhang, *Sens. Actuators B* **123**, 420 (2007)
40. F.K.M. Alosfur, N.J. Ridha, *Appl. Phys. A.* **127**, 203 (2021)
41. Y. Zhao, Xu. Sha Wang, L.S. Zhai, X. Bai, Y. Liu, T. Wang, Y. Li, L. Zhang, F. Fan, F. Meng, X. Zhang, Fu. Yu, *ACS Appl. Mater. Interfaces.* **13**, 9206 (2021)
42. H. Gao, J. Guo, Y. Li, C. Xie, X. Li, L. Liu, Y. Chen, P. Sun, F. Liu, X. Yan, F. Liu, G. Lu, *Sens. Actuators B* **284**, 305 (2019)
43. S. Zhu, Xu. Lin, S. Yang, X. Zhou, X. Chen, B. Dong, X. Bai, Lu. Geyu, H. Song, *J. Colloid Interface Sci.* **569**, 358 (2020)
44. Y. Lü, W. Zhan, Y. He, Y. Wang, X. Kong, Q. Kuang, Z. Xie, L. Zheng, *ACS Appl. Mater. Interfaces* **6**, 4186 (2014)
45. Xu. Lin, R. Zheng, S. Liu, J. Song, J. Chen, B. Dong, H. Song, *Inorg. Chem.* **51**, 7733 (2012)
46. X. Chen, Y. Shen, P. Zhou, X. Zhong, G. Li, C. Hana, D. Wei, S. Li, *Sens. Actuators B* **289**, 160 (2019)
47. L. Ma, H. Fan, H. Tian, J. Fang, X. Qian, *Sens. Actuators B* **222**, 508 (2016)
48. L. Sun, Y. Guo, Y. Hu, S. Pan, Z. Jiao, *Sens. Actuators B* **337**, 129793 (2021)
49. M. Yang, X. Zhang, X. Cheng, *ACS Appl. Mater. Interfaces.* **9**, 26293 (2017)
50. J. Xu, Z. Xue, N. Qin, Z. Cheng, Q. Xiang, *Sens. Actuators B* **242**, 148 (2017)

Publisher’s Note Springer Nature remains neutral with regard to jurisdictional claims in published maps and institutional affiliations.